






Application of an X-Ray Clumpy Torus Model (XCLUMPY) to 10 Obscured Active Galactic Nuclei Observed with Suzaku and NuSTAR

著者	Atsushi Tanimoto, Yoshihiro Ueda, Hirokazu Odaka, Shoji Ogawa, Satoshi Yamada, Toshihiro Kawaguchi, Kohei Ichikawa
journal or publication title	The Astrophysical Journal
volume	897
number	1
page range	2
year	2020-06-26
URL	http://hdl.handle.net/10097/00130851

doi: 10.3847/1538-4357/ab96bc



Application of an X-Ray Clumpy Torus Model (XCLUMPY) to 10 Obscured Active Galactic Nuclei Observed with Suzaku and NuSTAR

Atsushi Tanimoto^{1,2} , Yoshihiro Ueda¹ , Hirokazu Odaka^{2,3}, Shoji Ogawa¹ , Satoshi Yamada¹ , Toshihiro Kawaguchi⁴, and Kohei Ichikawa^{5,6} 

¹ Department of Astronomy, Kyoto University, Kyoto 606-8502, Japan; atsushi.tanimoto@phys.s.u-tokyo.ac.jp

² Department of Physics, The University of Tokyo, Tokyo 113-0033, Japan

³ Kavli IPMU (WPI), UTIAS, The University of Tokyo, Chiba 277-8583, Japan

⁴ Department of Economics, Management and Information Science, Onomichi City University, Hiroshima 722-8506, Japan

⁵ Frontier Research Institute for Interdisciplinary Sciences, Tohoku University, Miyagi 980-8578, Japan

⁶ Astronomical Institute, Tohoku University, Miyagi 980-8578, Japan

Received 2019 December 28; revised 2020 May 21; accepted 2020 May 25; published 2020 June 26

Abstract

We apply XCLUMPY, an X-ray spectral model from a clumpy torus in an active galactic nucleus (AGN), to the broadband X-ray spectra of 10 obscured AGNs observed with both Suzaku and NuSTAR. The infrared spectra of these AGNs were analyzed by Ichikawa et al. with the CLUMPY code. Because XCLUMPY adopts the same clump distribution as that in the CLUMPY, we can directly compare the torus parameters obtained from the X-ray spectra and those from the infrared spectra. The torus angular widths determined from the infrared spectra (σ_{IR}) are systematically larger than those from the X-ray data (σ_{X}); the difference ($\sigma_{\text{IR}} - \sigma_{\text{X}}$) correlates with the inclination angle determined from the X-ray spectrum. These results can be explained by the contribution from dusty polar outflows to the observed infrared flux, which becomes more significant at higher inclinations (more edge-on views). The ratio of the hydrogen column density to the V-band extinction in the line-of-sight absorber shows a large scatter ($\simeq 1$ dex) around the Galactic value, suggesting that a significant fraction of AGNs have dust-rich circumnuclear environments.

Unified Astronomy Thesaurus concepts: Active galactic nuclei (16); Astrophysical black holes (98); High energy astrophysics (739); Seyfert galaxies (1447); Supermassive black holes (1663); X-ray active galactic nuclei (2035)

1. Introduction

The unification model of an active galactic nucleus (AGN; Antonucci 1993; Urry & Padovani 1995; Netzer 2015; Ramos Almeida & Ricci 2017) indicates the ubiquitous presence of an obscuring dusty, molecular gas region (the so-called “torus”) around the accreting supermassive black hole (SMBH). The torus is a key structure for understanding the mechanisms of the coevolution between the SMBH and the host galaxy (Kormendy & Ho 2013; Heckman & Best 2014) because it is considered as a mass reservoir that feeds material onto the SMBH from the host galaxy. Nevertheless, the basic properties of the tori (e.g., spatial distribution of matter and the gas-to-dust ratio) are still unclear.

Many studies indicated that the torus consists of dusty clumps (clumpy torus: Krolik & Begelman 1988; Laor & Draine 1993; Höning et al. 2006; Höning & Beckert 2007; Nenkova et al. 2008a, 2008b; Höning et al. 2012). Nenkova et al. (2008a, 2008b) constructed an infrared spectral model from the clumpy torus called CLUMPY. They assumed a power-law distribution of clumps in the radial direction and a Gaussian distribution in the elevation direction. This CLUMPY model has been widely used to analyze the infrared spectra of AGNs (e.g., Ramos Almeida et al. 2009, 2011a, 2011b, 2011c, 2014b, 2014a; Alonso-Herrero et al. 2011, 2012a, 2012b, 2013; García-Bernete et al. 2015, 2019; Ichikawa et al. 2015; Fuller et al. 2016, 2019; Audibert et al. 2017; Mateos et al. 2017; Lopez-Rodriguez et al. 2018).

X-ray spectra of AGNs provide a powerful tool to study the properties of the tori. This is because X-rays (in particular hard X-rays above 10 keV) have strong penetrating power against absorption and can trace all material including gas and dust in

an unbiased manner, unlike the infrared continuum emission, which is sensitive only to dust. The torus produces a line-of-sight absorption of the primary emission and a reflected spectrum accompanied by fluorescence lines. These signals carry important information on the torus parameters (e.g., the hydrogen column density and the covering factor). In many previous studies, analytic reflection models, such as the pexrav model (Magdziarz & Zdziarski 1995), were used to approximate the torus-reflection component, although the assumed geometry and condition are too simple. To consider the complex geometry of a torus, several Monte Carlo-based numerical models have been developed (e.g., MYTorus model, Murphy & Yaqoob 2009; Ikeda model, Ikeda et al. 2009; boros02 model, Baloković et al. 2018). These models, however, assumed a uniform density torus (“smooth torus”), which is not realistic, as we mentioned above.

Following the earlier works by Liu & Li (2014) and Furu et al. (2016), Tanimoto et al. (2019) made a new X-ray spectral model from a clumpy torus called XCLUMPY,⁷ utilizing the Monte Carlo simulation for astrophysics and cosmology (MONACO; Odaka et al. 2011, 2016) framework. XCLUMPY assumes the same torus geometry of the clump distribution as that of the CLUMPY model (Nenkova et al. 2008a, 2008b). This enables us to directly compare the torus parameters obtained from the X-ray spectra and those from infrared spectra.

To date, XCLUMPY has been applied to the X-ray spectra of two Seyfert 1 galaxies (IC 4329A and NGC 7469; Ogawa

⁷ More recently, Buchner et al. (2019) have also published a similar model called UXCLUMPY.

et al. 2019) and one Compton-thick Seyfert 2 galaxy (the Circinus galaxy, Tanimoto et al. 2019). Interpretation of the results is somewhat puzzling, however. Tanimoto et al. (2019) found that the ratio of the hydrogen column density to the V -band extinction along the line of sight ($N_{\text{H}}^{\text{LOS}}/A_{\text{V}}^{\text{LOS}}$) in the Circinus galaxy is $\simeq 10$ times larger than that of the Galactic interstellar medium (ISM), while Ogawa et al. (2019) showed that they are $\simeq 2$ –70 times smaller than the Galactic value in IC 4329A and NGC 7469. To obtain an overview of AGN torus properties, we need to increase the number of AGNs whose spectra are analyzed with the XCLUMPY model.

This paper presents the results of applications of XCLUMPY to the broadband X-ray spectra of 10 obscured AGNs observed with both Suzaku and NuSTAR. The structure of this paper is organized as follows. Section 2 describes our sample and the data reduction. Section 3 presents the X-ray spectral analysis using XCLUMPY. Section 4 summarizes the results. In Section 5, we compare the torus parameters obtained from the X-ray spectra and those from the infrared data. We assume the solar abundances of Anders & Grevesse (1989). To estimate the luminosity, we adopt the cosmological parameters of $H_0 = 70.0 \text{ km s}^{-1} \text{ Mpc}^{-1}$, $\Omega_{\text{m}} = 0.30$, and $\Omega_{\lambda} = 0.70$. The error on a spectral parameter corresponds to the 90% confidence limit for a single parameter estimated using the Markov Chain Monte Carlo method.

2. Sample and Data Analysis

2.1. Sample

Our sample is taken from that of Ichikawa et al. (2015).⁸ They compiled high-spatial-resolution mid-infrared N -band spectroscopy, Q -band imaging, and nuclear near- and mid-infrared photometries from Alonso-Herrero et al. (2011) and González-Martín et al. (2013) for 21 nearby AGNs. By applying the CLUMPY model to the infrared spectra, Ichikawa et al. (2015) examined torus properties such as the V -band extinction of the torus (A_{V}) along the equatorial plane, the torus angular width (σ_{IR}), and the inclination angle (i_{IR}).

In this paper, we analyze the broadband X-ray spectra of 10 obscured AGNs ($\log N_{\text{H}}/\text{cm}^{-2} \geq 22$) observed with both Suzaku and NuSTAR among the 21 objects in Ichikawa et al. (2015). In a later discussion, we also include the Circinus galaxy and NGC 5135, for which Tanimoto et al. (2019) and Yamada et al. (2020) published the X-ray analysis results utilizing XCLUMPY, respectively. We have excluded three objects from the Ichikawa et al. (2015) sample that show very complex X-ray spectra: (1) NGC 1068, a heavily Compton-thick AGN whose X-ray spectrum is dominated by photo-ionized plasma emission (e.g., Kallman et al. 2014), (2) NGC 1386, which exhibited strong spectral variability between the Suzaku and NuSTAR observations according to our analysis, and (3) Cen A, which may contain a jet component (e.g., Fukazawa et al. 2011). We focus on obscured AGNs because the line-of-sight absorption can be used to constrain the torus parameters (unless the absorption by the host galaxy is significant). High-quality broadband X-ray spectra, like those of Suzaku and NuSTAR, are essential for separating and characterizing the torus-reflection component. Tables 1 and 2 summarize our sample and the observations, respectively.

⁸ The analysis of broadband X-ray spectra including the new sample of García-Berete et al. (2019) will be reported in a forthcoming paper (S. Ogawa et al. 2020, in preparation).

2.2. Data Analysis

2.2.1. Suzaku

Suzaku (2005–2015) is the fifth Japanese X-ray astronomical satellite (Mitsuda et al. 2007). It carried four CCD cameras called the X-ray imaging spectrometers (XIS0, XIS1, XIS2, XIS3; Koyama et al. 2007) and collimated hard X-ray instrument called the hard X-ray detector (HXD; Takahashi et al. 2007). XIS1 is a back-illuminated CCD (BIXIS) sensitive to 0.2–12.0 keV photons, and XIS0, XIS2, and XIS3 are front-side-illuminated ones (FIXIS) sensitive to 0.4–12.0 keV photons. HXD consists of the PIN photodiodes (PIN) covering the 10–70 keV band and the gadolinium silicon oxide (GSO) scintillation counters covering the 40–600 keV band (Kokubun et al. 2007).

We analyzed the XIS and HXD-PIN data with HEASoft 6.26 and the calibration database (CALDB) released on 2018 October 10 (XIS) and 2011 September 13 (HXD). The XIS and HXD data were reprocessed by using aepipeline. We extracted the source spectrum of the XIS from a $1'$ radius circular region centered on the source peak and the background from a $1'$ radius source-free region. We generated the redistribution matrix files (RMF) with xisrmfgen and the ancillary response files (ARF) with xissimarfgen (Ishisaki et al. 2007). The source spectrum, the background spectrum, the RMF, and the ARF of FIXIS were combined with addascaspec. We created the HXD/PIN spectrum with hxdpinxbpi. We utilized the tuned background files (Fukazawa et al. 2009) to reproduce the non-X-ray background (NXB). The simulated spectrum of the cosmic X-ray background (CXB) was added to the NXB.

2.2.2. NuSTAR

NuSTAR (2012–) is the first imaging satellite in the hard X-ray band above 10 keV (Harrison et al. 2013). It carries two coaligned grazing incidence telescopes coupled with two focal plane modules (FPMs) and covers the energy band of 3–79 keV. We analyzed the FPM data with HEASoft 6.26 and CALDB released on 2019 April 10. The FPM data were reprocessed by using nupipeline. We extracted the source spectrum from a $1'$ radius circular region centered on the source peak and the background from a $1'$ radius source-free region, using the nuproducts script. The source spectrum, the background spectrum, the RMF, and the ARF were combined with addascaspec.

3. Spectral Analysis

We employ the XCLUMPY model to reproduce the reflection spectra from the torus. The torus geometry of the clump distribution is the same as that of the CLUMPY model (Nenkova et al. 2008a, 2008b) i.e., a power-law distribution in the radial direction and a normal distribution in the elevation direction. The number density function $d(r, \theta, \phi)$ (in units of pc^{-3}) is represented in the spherical coordinate system (where r is the radius, i is the inclination angle measured from the rotation axis, and ϕ is the azimuth) as

$$d(r, \theta, \phi) = N \left(\frac{r}{r_{\text{in}}} \right)^{-1/2} \exp \left(-\frac{(i - \pi/2)^2}{\sigma^2} \right), \quad (1)$$

where N is the normalization, r_{in} is the inner radius of the torus, and σ is the torus angular width around the midplane

Table 1
Information on Objects

Galaxy Name (1)	Classification (2)	R.A. (3)	Decl. (4)	Redshift (5)	$N_{\text{H}}^{\text{Gal}}$ (6)
IC 5063	Seyfert 2.0	20 ^h 52 ^m 02 ^s .34	−57 ^d 04 ^m 07 ^s .6	0.01135	0.07390
NGC 2110	Seyfert 2.0	05 ^h 52 ^m 11 ^s .38	−07 ^d 27 ^m 22 ^s .4	0.00779	0.29800
NGC 3227	Seyfert 2.0	10 ^h 23 ^m 30 ^s .58	+19 ^d 51 ^m 54 ^s .2	0.00386	0.02130
NGC 3281	Seyfert 2.0	10 ^h 31 ^m 52 ^s .09	−34 ^d 51 ^m 13 ^s .3	0.01067	0.08940
NGC 5506	Seyfert 1.9	14 ^h 13 ^m 14 ^s .89	−03 ^d 12 ^m 27 ^s .3	0.00618	0.04890
NGC 5643	Seyfert 2.0	14 ^h 32 ^m 40 ^s .74	−44 ^d 10 ^m 27 ^s .8	0.00400	0.12400
NGC 5728	Seyfert 2.0	14 ^h 42 ^m 23 ^s .89	−17 ^d 15 ^m 11 ^s .1	0.00935	0.10000
NGC 7172	Seyfert 2.0	22 ^h 02 ^m 01 ^s .89	−31 ^d 52 ^m 10 ^s .8	0.00868	0.02120
NGC 7582	Seyfert 2.0	23 ^h 18 ^m 23 ^s .50	−42 ^d 22 ^m 14 ^s .0	0.00525	0.01390
NGC 7674	Seyfert 2.0	23 ^h 27 ^m 56 ^s .72	+08 ^d 46 ^m 44 ^s .5	0.02892	0.05200

Note. Column (1): galaxy name. Column (2): optical classification from the NASA/IPAC extragalactic database (NED). Column (3): R.A. from the NED. Column (4): decl. from the NED. Column (5) redshift from the NED. Column (6): total Galactic H I and H₂ values in units of 10²² cm^{−2} (Willingale et al. 2013).

(Tanimoto et al. 2019). The inner and outer radii of the torus and the radius of each clump is set to be 0.05 pc, 1.00 pc, and 0.002 pc,⁹ respectively. This model has five free parameters: (1) hydrogen column density along the equatorial plane ($N_{\text{H}}^{\text{Equ}}$: 10²³–10²⁶ cm^{−2}), (2) torus angular width (σ : 10°–70°), (3) inclination angle (i : 20°–87°), (4) photon index (Γ : 1.5–2.5), and (5) cutoff energy (E_{cut} : 10¹–10³ keV).

For each object, we perform simultaneous fitting to the Suzaku/BIXIS (0.5–8.0 keV), Suzaku/FIXIS (2–10 keV), Suzaku/HXD (16–40 keV; the widest case), and NuSTAR/FPM (8–60 keV; the widest case) spectra. Our model is represented as follows in XSPEC (Arnaud 1996) terminology:

const1 * phabs

$$\begin{aligned} & *(\text{const2} * \text{zphabs} * \text{cabs} * \text{zcutoffpl} \\ & + \text{const3} * \text{zcutoffpl} + \text{atable}\{\text{xclumpy_R.fits}\} \\ & + \text{const4} * \text{atable}\{\text{xclumpy_L.fits}\} + \text{apec} \end{aligned} \quad (2)$$

This model consists of six components:

1. **const1*phabs.** The const1 term is a cross-normalization constant to adjust small differences in the absolute flux calibration among different instruments. We set those of Suzaku/FIXIS and NuSTAR/FPM to unity as references. That of Suzaku/HXD is set to 1.16 (for the XIS-nominal pointing position) or 1.18 (HXD nominal). We leave that of Suzaku/BIXIS (C_{BIXIS}) as a free parameter. The phabs term represents the Galactic absorption. We fix the hydrogen column density to the total Galactic H I and H₂ values provided by Willingale et al. (2013).
2. **const2*zphabs*cabs*zcutoffpl.** This component represents the transmitted continuum through the torus. The const2 term (C_{Time}) is a constant to consider time variability between the Suzaku and NuSTAR observations. We do not multiply this constant to the scattered component and the reflection component. This is because the sizes of the scatterer and reflector are most likely parsec or larger scales and hence little time variability is expected. We limit the C_{Time} value within a range of 0.10–10.0 to avoid unrealistic results (e.g., Kawamuro et al. 2016a; Tanimoto et al. 2018). The zphabs and cabs

terms represent the photoelectric absorption¹⁰ and Compton scattering by the torus, respectively. The hydrogen column density along the line of sight ($N_{\text{H}}^{\text{LOS}}$) is determined according to Equation (3) (see below). The zcutoffpl is the intrinsic continuum modeled by a power law with an exponential cutoff. Because it is difficult to determine the cutoff energy, we fix this at a typical value ($E_{\text{cut}} = 370$ keV; Ricci et al. 2018).

3. **const3*zcutoffpl.** This represents the scattered component, where const3 is the scattering fraction (f_{scat}). We link the photon index (Γ), the cutoff energy (E_{cut}), and the normalization (N_{Dir}) to those of the intrinsic continuum.
4. **xclumpy_R.fits.** This component represents the reflection continuum from the torus based on XCLUMPY. XCLUMPY has six free parameters: $N_{\text{H}}^{\text{Equ}}$, σ , i , Γ , E_{cut} , and N_{Dir} . We link Γ , E_{cut} , and N_{Dir} to those of the intrinsic continuum. The line-of-sight absorption $N_{\text{H}}^{\text{LOS}}$ is related to torus parameters as follows:

$$N_{\text{H}}^{\text{LOS}} = \alpha N_{\text{H}}^{\text{Equ}} \exp\left(-\frac{(i - \pi/2)^2}{\sigma^2}\right). \quad (3)$$

Here, the dimensionless factor α is introduced to take into account a possible statistical fluctuation in the number of clumps along the line of sight. To avoid unrealistic solutions, we limit α within the range of 0.5–2.0 (i.e., a factor of 2); this is because a typical clump number along the line of sight is found to be $\simeq 4$ in our analysis, whose fractional standard deviation assuming the Poisson distribution is $\simeq 50\%$. When the error of the inclination angle is greater than 30°, we fix it to the value obtained from the infrared data (for NGC 3227, NGC 5643, and NGC 5728).

5. **const4*xclumpy_L.fits.** This component represents fluorescence lines from the torus based on XCLUMPY. The const4 term is a relative normalization (N_{Line}) to consider possible systematic uncertainties. For instance, recent studies implied contribution from spatially extended fluorescence lines (Arévalo et al. 2014; Bauer et al. 2015; Fabbiano et al. 2017; Kawamuro et al. 2019). We link $N_{\text{H}}^{\text{Equ}}$, σ , i , Γ , and E_{cut} to those of the reflection continuum.

⁹ The absolute numbers of these three parameters are arbitrary and only their ratios are important, because a self-similar geometry produces identical results.

¹⁰ The differences in the absorption cross section between the zphabs model and that utilized in XCLUMPY (xraylib; Schoonjans et al. 2011) are almost negligible at energies above 1 keV.

Table 2
Summary of Observations

Galaxy Name (1)	Observatory (2)	Observation ID (3)	Start Date (4)	End Date (5)	Exposure (6)	Binning (7)	Reference (8)
IC 5063	Suzaku	704010010	2009 Apr 24	2009 Apr 25	45	50	(01)
	NuSTAR	60061302002	2013 Jul 8	2013 Jul 8	18	50	(02)
NGC 2110	Suzaku	707034010	2012 Aug 31	2012 Sep 2	103	100	(03) (04)
	NuSTAR	60061061002	2012 Oct 5	2012 Oct 5	16	100	(02) (05)
NGC 3227	Suzaku	703022050	2008 Nov 27	2008 Nov 29	79	50	(06)
	NuSTAR	60202002002	2016 Nov 9	2016 Nov 10	49	50	...
NGC 3281	Suzaku	703033010	2008 May 21	2008 May 23	46	50	...
	NuSTAR	60061201002	2016 Jan 22	2016 Jan 23	22	50	...
NGC 5506	Suzaku	701030030	2007 Jan 31	2007 Feb 1	57	100	(04)
	NuSTAR	60061323002	2014 Apr 1	2014 Apr 3	56	100	(07)
NGC 5643	Suzaku	702010010	2007 Aug 19	2007 Aug 20	43	50	(08)
	NuSTAR	60061362002	2014 May 24	2014 May 25	22	50	(09)
NGC 5728	Suzaku	701079010	2006 Jun 19	2006 Jun 20	41	50	(10)
	NuSTAR	60061256002	2013 Jan 2	2013 Jan 2	24	50	(09)
NGC 7172	Suzaku	703030010	2008 May 25	2008 May 26	82	100	(04)
	NuSTAR	60061308002	2014 Oct 7	2014 Oct 8	32	100	...
NGC 7582	Suzaku	702052040	2007 Nov 16	2007 Nov 16	32	50	(10) (11)
	NuSTAR	60201003002	2016 Apr 28	2016 Apr 29	47	50	(02) (09)
NGC 7674	Suzaku	708023010	2013 Dec 8	2013 Dec 10	52	50	(12)
	NuSTAR	60001151002	2014 Sep 30	2014 Oct 1	50	50	(12)

Note. Column (1): galaxy name. Column (2): observatory. Column (3): observation identification number. Column (4): start date in units of ymd. Column (5): end date in units of ymd. Column (6): exposure in units of ks. Here we adopt Suzaku/XIS0 and NuSTAR/FPMA exposures. Column (7): binning. Column (8): references for the previous work

References. (01) Tazaki et al. (2011). (02) Baloković et al. (2018). (03) Rivers et al. (2014). (04) Kawamuro et al. (2016a). (05) Marinucci et al. (2015). (06) Noda et al. (2014). (07) Matt et al. (2015). (08) Kawamuro et al. (2016b). (09) Marchesi et al. (2019). (10) Tanimoto et al. (2018). (11) Bianchi et al. (2009). (12) Gandhi et al. (2017).

6. *apec*. This component represents emission from an optically thin thermal plasma in the host galaxy. We adopt it when the improvement of the fit by adding this component is significant at a >99% confidence level with the F-test.¹¹

4. Results

Figure 1 shows the folded X-ray spectra and the best-fitting models. Table 3 summarizes the best-fitting parameters. Table 4 gives the observed fluxes, the intrinsic luminosities, and the Eddington ratios. Here we estimate the bolometric luminosity as $L_{\text{Bol}} = 20L_{2-10\text{keV}}$, where $L_{2-10\text{keV}}$ is the intrinsic 2–10 keV luminosity, and define the Eddington luminosity as $L_{\text{Edd}} = 1.25 \times 10^{38} M_{\text{BH}}/M_{\odot}$, where M_{BH} is the black hole mass. Below, we compare our results with previous studies where different reflection models were adopted. To focus on differences in the spectral models, not in the data, here we only refer to previous works that utilized Suzaku or NuSTAR data.

4.1. IC 5063

The model with an *apec* component reproduces the broadband (0.50–60.0 keV) X-ray spectrum ($\chi_{\text{red}}^2 = 0.97$) well. We obtain $N_{\text{H}}^{\text{LOS}} = 0.26_{-0.14}^{+0.49} \times 10^{24} \text{ cm}^{-2}$ and $\Gamma = 1.89_{-0.09}^{+0.10}$. Our best-fitting parameters are consistent with the Suzaku results (Tazaki et al. 2011) and the NuSTAR results (Baloković et al. 2018). Tazaki et al. (2011) estimated $N_{\text{H}}^{\text{LOS}} = 0.25_{-0.01}^{+0.10} \times 10^{24} \text{ cm}^{-2}$ and $\Gamma = 1.82_{-0.11}^{+0.08}$ with the Ikeda model. Baloković et al. (2018)

obtained $N_{\text{H}}^{\text{LOS}} = 0.21 \times 10^{24} \text{ cm}^{-2}$ and $\Gamma = 1.75$ with the *borus02* model.

4.2. NGC 2110

The model without an *apec* component is able to reproduce the broadband (0.50–60.0 keV) X-ray spectrum ($\chi_{\text{red}}^2 = 1.03$). Our best-fitting parameters are $N_{\text{H}}^{\text{LOS}} = 0.04_{-0.01}^{+0.01} \times 10^{24} \text{ cm}^{-2}$ and $\Gamma = 1.63_{-0.01}^{+0.01}$. Our results agree with the Suzaku results (Rivers et al. 2014; Kawamuro et al. 2016a) and the NuSTAR results (Marinucci et al. 2015; Baloković et al. 2018). Utilizing the *pexrav* model (Magdziarz & Zdziarski 1995) for the reflection component, Rivers et al. (2014) obtained $N_{\text{H}}^{\text{LOS}} = 0.05_{-0.01}^{+0.01} \times 10^{24} \text{ cm}^{-2}$ and $\Gamma = 1.66_{-0.01}^{+0.01}$, and Kawamuro et al. (2016a) obtained $N_{\text{H}}^{\text{LOS}} = 0.02_{-0.01}^{+0.01} \times 10^{24} \text{ cm}^{-2}$ and $\Gamma = 1.65_{-0.01}^{+0.01}$. Marinucci et al. (2015) obtained $N_{\text{H}}^{\text{LOS}} = 0.04_{-0.01}^{+0.01} \times 10^{24} \text{ cm}^{-2}$ and $\Gamma = 1.64_{-0.03}^{+0.03}$ with the *MYTorus* model, and Baloković et al. (2018) obtained $N_{\text{H}}^{\text{LOS}} = 0.04 \times 10^{24} \text{ cm}^{-2}$ and $\Gamma = 1.63$ with the *borus02* model.

4.3. NGC 3227

The NuSTAR data are reported for the first time. The model without an *apec* component provides an adequate fit ($\chi_{\text{red}}^2 = 1.22$). We obtain $N_{\text{H}}^{\text{LOS}} = 0.07_{-0.02}^{+0.01} \times 10^{24} \text{ cm}^{-2}$ and $\Gamma = 1.58_{-0.02}^{+0.03}$. These are consistent with the Suzaku results by Noda et al. (2014; $N_{\text{H}}^{\text{LOS}} = 0.10_{-0.01}^{+0.01} \times 10^{24} \text{ cm}^{-2}$ and $\Gamma = 1.67_{-0.06}^{+0.06}$) utilizing the *pexrav* model.¹²

¹¹ Note that this approach is an approximation because the F-test is known to be invalid when the simpler model is at the border of the parameter space of the more complex model (Protassov et al. 2002).

¹² Among the total six Suzaku observations analyzed by Noda et al. (2014), we analyze the data of the fifth observation, which has the longest exposure.

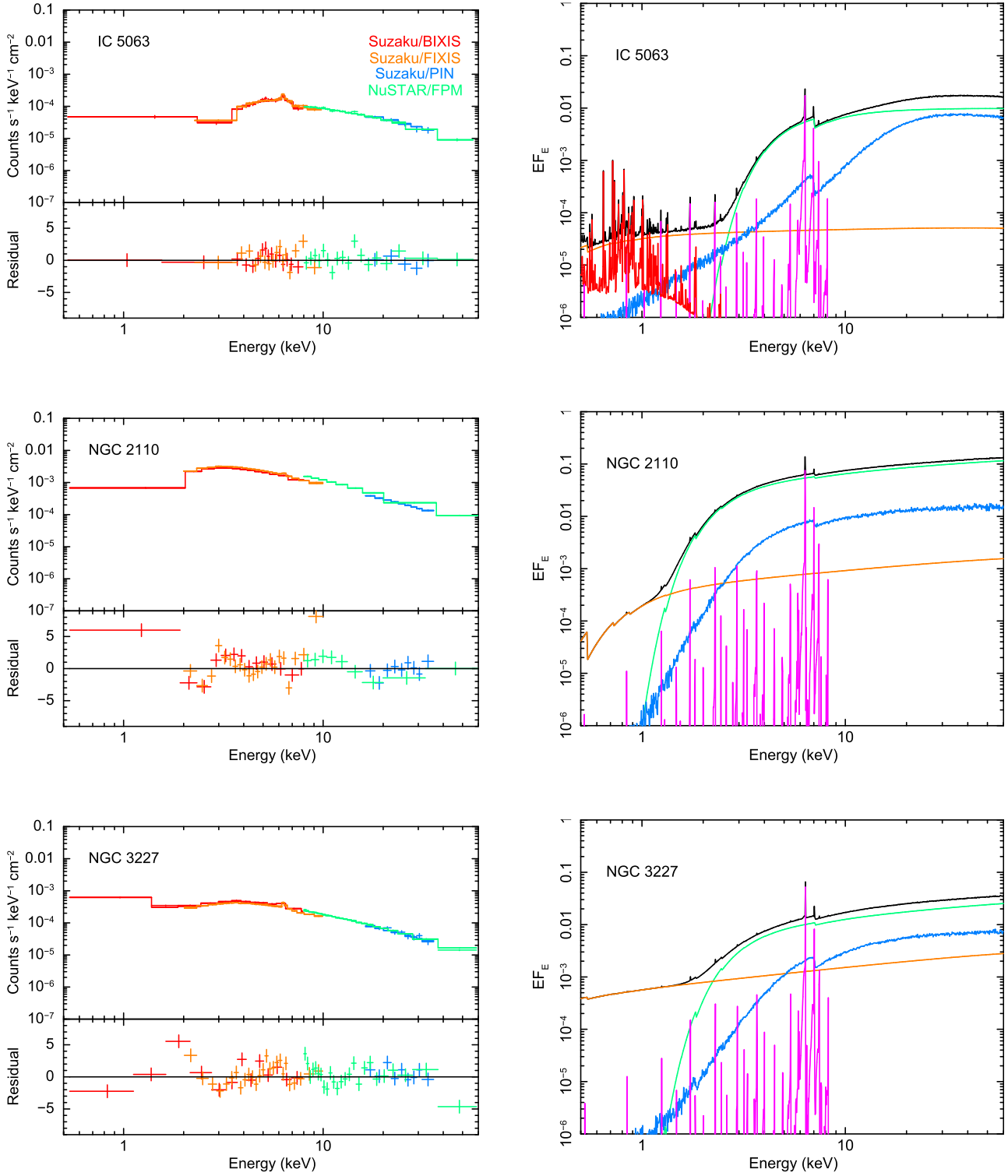


Figure 1. Left: the folded X-ray spectra fitted with XCLUMPY. Red crosses: Suzaku/BIXIS. Orange crosses: Suzaku/FIXIS. Blue crosses: Suzaku/PIN. Green crosses: NuSTAR/FPM. Solid curves: the best-fitting model. Lower panel: the residuals. Right: the best-fitting models. Black line: total. Red line: thermal emission from optically thin plasma. Orange line: scattered component. Green line: direct component. Blue line: reflection continuum from the torus. Magenta line: emission lines from the torus.

4.4. NGC 3281

The NuSTAR data are reported for the first time. The model with an apec component provides an adequate fit ($\chi^2_{\text{red}} = 1.23$). Our best-fitting parameters are $N_{\text{H}}^{\text{LOS}} = 0.66^{+0.38}_{-0.17} \times 10^{24} \text{ cm}^{-2}$ and $\Gamma = 1.50^{+0.05}$. We note that α is pegged at the upper boundary (2.0).

4.5. NGC 5506

The model with an apec component reproduces the broadband (0.60–60.0 keV) X-ray spectrum ($\chi^2_{\text{red}} = 1.08$) well. We obtain $N_{\text{H}}^{\text{LOS}} = 0.03^{+0.01}_{-0.01} \times 10^{24} \text{ cm}^{-2}$ and $\Gamma = 1.84^{+0.02}_{-0.01}$. Our photon index is slightly smaller than those of Suzaku (Kawamuro et al. 2016a) and NuSTAR (Matt et al. 2015), while the column

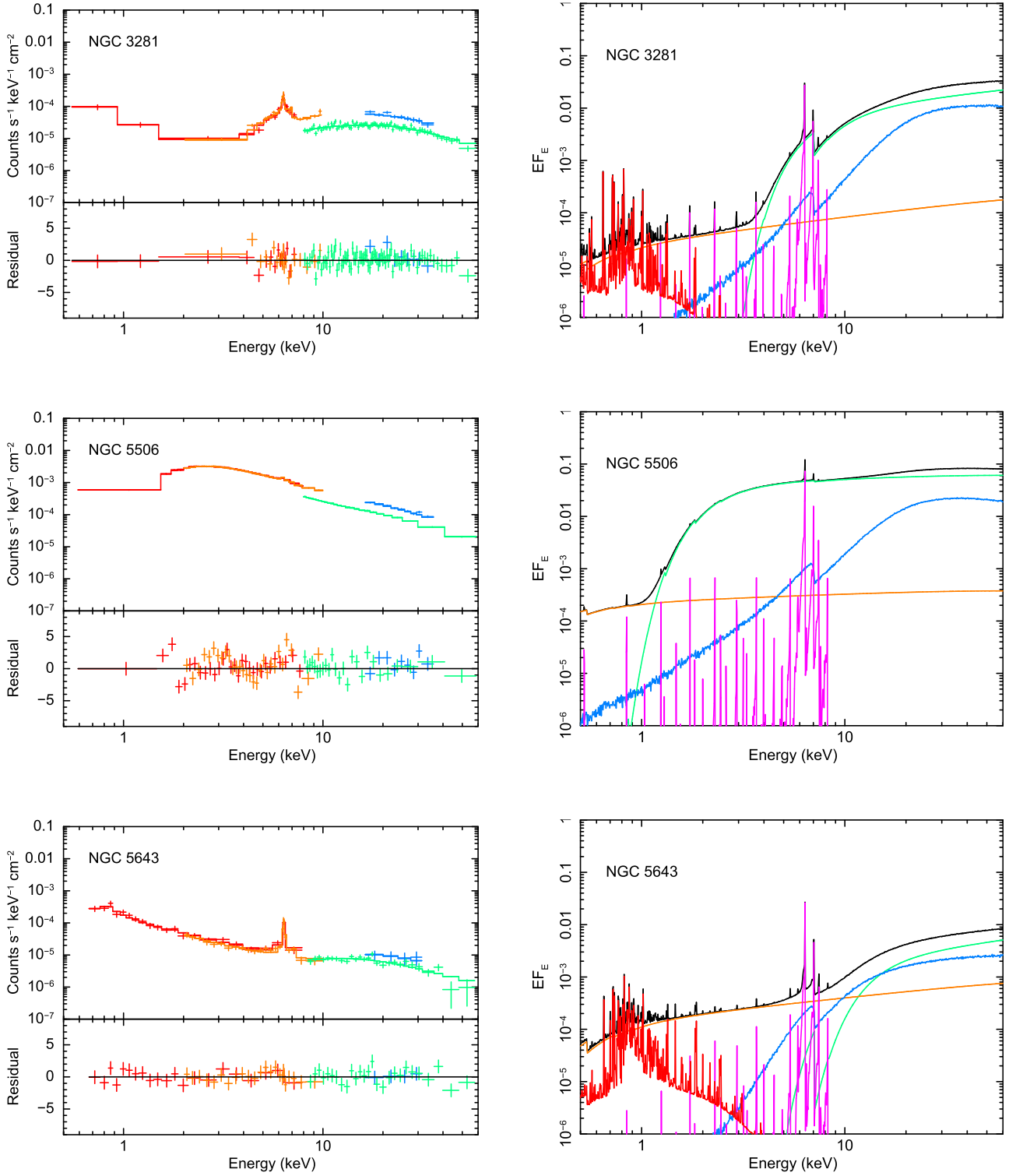


Figure 1. (Continued.)

density is consistent with their results. Kawamuro et al. (2016a) estimated $N_{\text{H}}^{\text{LOS}} = 0.03^{+0.01}_{-0.01} \times 10^{24} \text{ cm}^{-2}$ and $\Gamma = 1.95^{+0.01}_{-0.01}$ by applying the pexrav model to the reflection continuum. Matt et al. (2015) obtained $N_{\text{H}}^{\text{LOS}} = 0.03^{+0.01}_{-0.01} \times 10^{24} \text{ cm}^{-2}$ and $\Gamma = 1.91^{+0.03}_{-0.03}$ with the xillver model (García et al. 2013), which represents a reflection component from an illuminated accretion disk. We interpret that this is because XCLUMPY contains more

unabsorbed (hence softer) reflected continuum than the pexrav model (see Tanimoto et al. 2019, Section 4.3), resulting in a harder intrinsic continuum.

4.6. NGC 5643

The model with an apec component fits the broadband (0.70–55.0 keV) X-ray spectrum ($\chi^2_{\text{red}} = 0.99$) well. Our

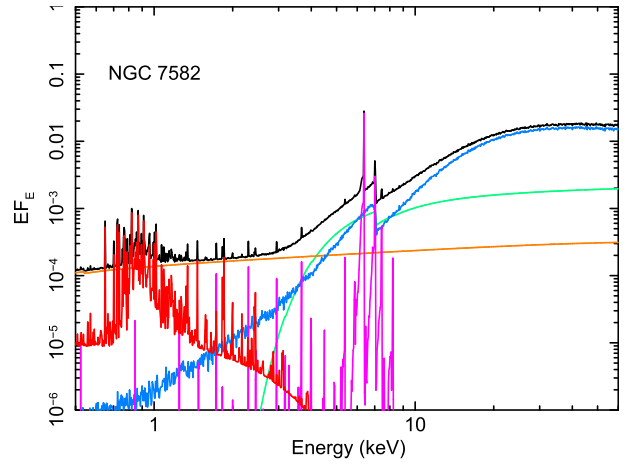
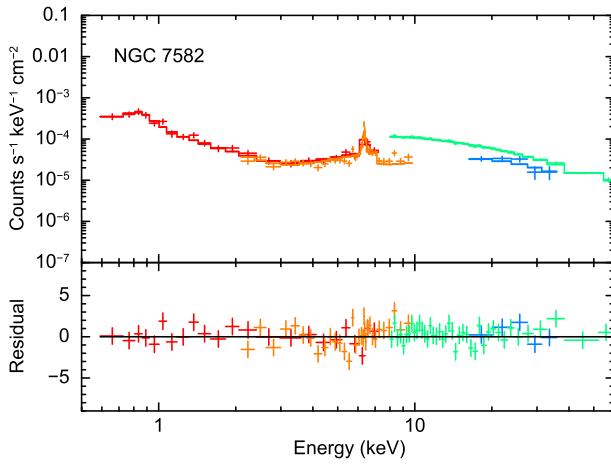
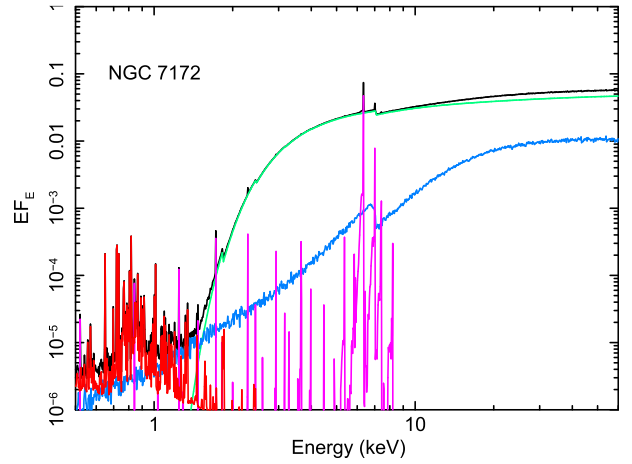
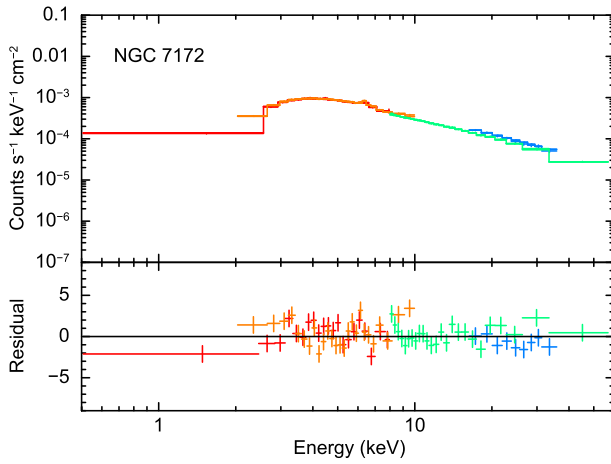
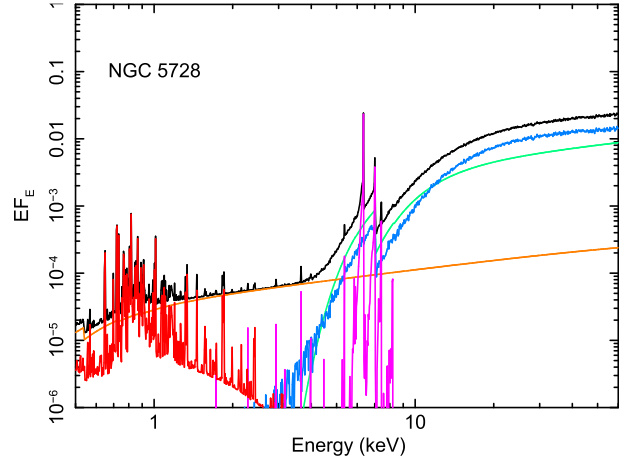
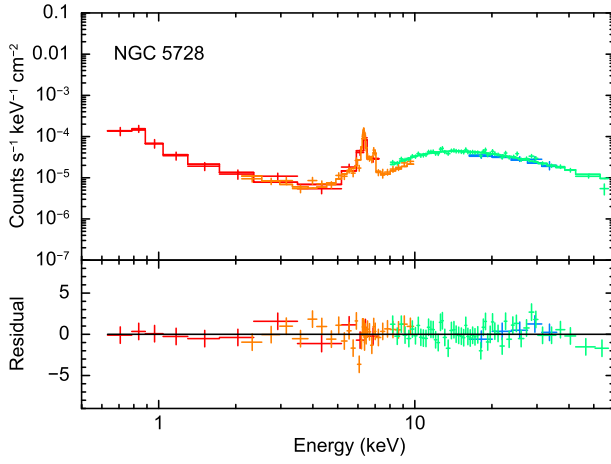


Figure 1. (Continued.)

best-fitting parameters are $N_{\text{H}}^{\text{LOS}} = 2.36^{+2.24}_{-0.58} \times 10^{24} \text{ cm}^{-2}$ and $\Gamma = 1.68^{+0.18}_{-0.17}$. Our results agree with the Suzaku results (Kawamuro et al. 2016b) and NuSTAR results (Marchesi et al. 2019). Kawamuro et al. (2016b) estimated $N_{\text{H}}^{\text{LOS}} = 0.94^{+0.61}_{-0.32} \times 10^{24} \text{ cm}^{-2}$ and $\Gamma = 1.57^{+0.37}_{-0.31}$ by employing the pexrav model. Marchesi et al. (2019) obtained $N_{\text{H}}^{\text{LOS}} = 2.69^{+1.88}_{-0.65} \times 10^{24} \text{ cm}^{-2}$ and $\Gamma = 1.55^{+0.13}_{-0.15}$ with the borus02 model.

4.7. NGC 5728

The model with an apc component reproduces the broadband (0.60–55.0 keV) X-ray spectrum ($\chi^2_{\text{red}} = 1.00$) well. We obtain $N_{\text{H}}^{\text{LOS}} = 0.95^{+0.29}_{-0.19} \times 10^{24} \text{ cm}^{-2}$ and $\Gamma = 1.50^{+0.05}$. Our photon index is slightly smaller than that from Suzaku (Tanimoto et al. 2018) and NuSTAR (Marchesi et al. 2019), whereas the hydrogen column density is consistent with their results. Tanimoto

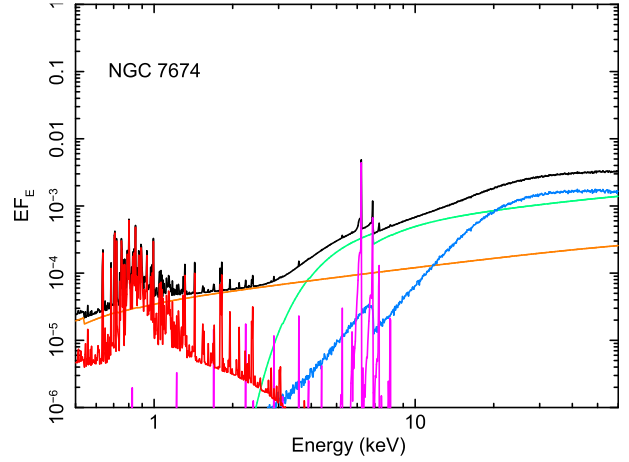
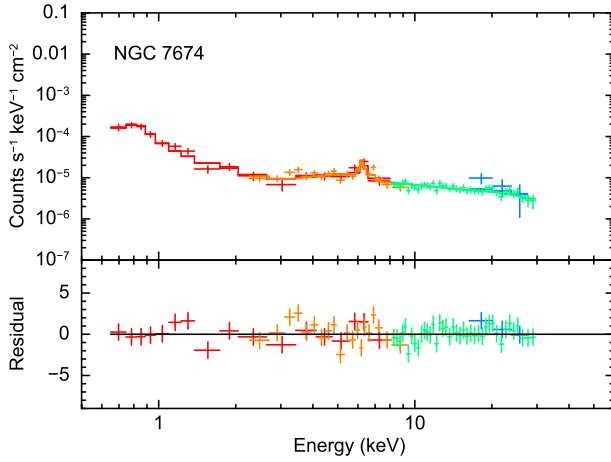


Figure 1. (Continued.)

et al. (2018) obtained $N_{\text{H}}^{\text{LOS}} = 1.69^{+1.45}_{-0.53} \times 10^{24} \text{ cm}^{-2}$ and $\Gamma = 1.69^{+0.14}_{-0.14}$ by applying the Ikeda model,¹³ and Marchesi et al. (2019) obtained $N_{\text{H}}^{\text{LOS}} = 0.96^{+0.05}_{-0.03} \times 10^{24} \text{ cm}^{-2}$ and $\Gamma = 1.81^{+0.07}_{-0.04}$ with the boros02 model. This trend is the same as the case of NGC 5506. It can be explained by a large unabsorbed reflection-continuum flux in the XCLUMPY model.

4.8. NGC 7172

The NuSTAR data are reported for the first time. The model with an apec component replicates the broadband (0.50–60.0 keV) X-ray spectrum ($\chi_{\text{red}}^2 = 1.02$) well. Our best-fitting parameters are $N_{\text{H}}^{\text{LOS}} = 0.09^{+0.18}_{-0.02} \times 10^{24} \text{ cm}^{-2}$ and $\Gamma = 1.76^{+0.02}_{-0.02}$. Our results agree with the Suzaku results of Kawamuro et al. (2016a), who obtained $N_{\text{H}}^{\text{LOS}} = 0.09^{+0.01}_{-0.01} \times 10^{24} \text{ cm}^{-2}$ and $\Gamma = 1.74^{+0.01}_{-0.02}$ by applying the pexrav model to the reflection continuum.

4.9. NGC 7582

The model with an apec component fits the broadband (0.60–60.0 keV) X-ray spectrum ($\chi_{\text{red}}^2 = 1.11$) well. We obtain $N_{\text{H}}^{\text{LOS}} = 0.31^{+0.16}_{-0.13} \times 10^{24} \text{ cm}^{-2}$ and $\Gamma = 1.77^{+0.08}_{-0.07}$. Analyzing the same Suzaku data with the Ikeda model, Tanimoto et al. (2018) obtained $N_{\text{H}}^{\text{LOS}} = 0.71^{+0.67}_{-0.15} \times 10^{24} \text{ cm}^{-2}$ and $\Gamma = 1.80^{+0.09}_{-0.10}$ (“Ikeda1” model) or $N_{\text{H}}^{\text{LOS}} = 3.23^{+1.33}_{-1.78} \times 10^{24} \text{ cm}^{-2}$ and $\Gamma = 1.88^{+0.11}_{-0.12}$ (“Ikeda2” model). Our XCLUMPY results prefer the previous model for this object (i.e., a Compton-thin AGN). Baloković et al. (2018) derived $N_{\text{H}}^{\text{LOS}} = 0.44 \times 10^{24} \text{ cm}^{-2}$ and $\Gamma = 1.67$ from the NuSTAR data by applying the boros02 model, which are similar to our results. We note that the time variability constant (C_{Time}) is pegged at 0.1, implying a large time variability in the transmitted component between the Suzaku and NuSTAR observations. It may be a result of a change in the line-of-sight absorption as reported by Bianchi et al. (2009).

4.10. NGC 7674

The model with an apec component gives an adequate fit ($\chi_{\text{red}}^2 = 1.20$). The best-fitting parameters are $N_{\text{H}}^{\text{LOS}} = 0.24^{+0.22}_{-0.10} \times 10^{24} \text{ cm}^{-2}$ and $\Gamma = 1.50^{+0.07}$. Our results are

consistent with the NuSTAR results of Gandhi et al. (2017), who obtained $N_{\text{H}}^{\text{LOS}} = 0.13^{+0.03}_{-0.03} \times 10^{24} \text{ cm}^{-2}$ and $\Gamma = 1.40^{+0.08}$ with the decoupled MYTorus model.

5. Discussion

5.1. Self-consistency of Our X-Ray Spectral Model

We have shown that the broadband X-ray spectra of the 10 nearby obscured AGNs can be reproduced well by employing the XCLUMPY model. XCLUMPY has only three free torus parameters: the hydrogen column density along the equatorial plane $N_{\text{H}}^{\text{Equ}}$, the torus angular width σ_{X} , and the inclination i_{X} . To make the spectral model self-consistent, the line-of-sight column density of the transmitted component has been linked to the torus parameters through Equation (3).

Here we have introduced a correction factor α , within a range of 0.5–2.0, to take into account a possible fluctuation in the line-of-sight absorption. We find that in 7 out of the 10 sources, the 90% confidence range of α contains unity (Table 3), meaning that the torus geometry assumed in XCLUMPY is consistent with the data. In the remaining three sources, NGC 2110, NGC 5643, and NGC 5728, α is pegged at either of the boundary values (0.5 or 2.0). The small sample size makes it difficult to judge if it is purely a result of statistical fluctuation in the clump number in the line of sight. Instead, it is possible that the actual matter distribution is not as simple as in the XCLUMPY geometry. For instance, we would observe a large α value when only a single optically thick cloud is present at the line of sight. A small α value would be expected if matter were more sharply concentrated in the equatorial plane than the Gaussian distribution. These limitations in using the XCLUMPY model must be always kept in mind when interpreting the results.

We have confirmed that our conclusions presented below do not change when we fix $\alpha = 1$ and are robust against parameter coupling among the torus parameters ($N_{\text{H}}^{\text{Equ}}$, σ_{X} , and i_{X}). Finally, we note that our spectral model ignores a possible time variability in the line-of-sight column density among different epochs, which may be the case for NGC 7582 (Section 4.9).

5.2. Comparison of Torus Parameters Obtained from X-Ray and Infrared Spectra

In this subsection, we compare the torus parameters obtained from the X-ray spectra and those from the infrared spectra.

¹³ Tanimoto et al. (2018) considered two models, “Ikeda1” and “Ikeda2,” where the line-of-sight absorption is linked and not linked to the torus parameters, respectively. Here we refer to the results of “Ikeda2.”

Table 3
Best-fitting Parameters

Galaxy Name (01)	C_{BIXIS} (02)	C_{Time} (03)	Γ (04)	N_{Dir} (05)	f_{scat} (06)	$N_{\text{H}}^{\text{LOS}}$ (07)	α (08)
	$N_{\text{H}}^{\text{Equ}}$ (09)	σ (10)	i (11)	N_{Line} (12)	$k_{\text{B}}T$ (13)	$N_{k_{\text{B}}T}$ (14)	χ_{red}^2 (15)
IC 5063	$0.96_{-0.04}^{+0.04}$	$0.87_{-0.04}^{+0.04}$	$1.89_{-0.10}^{+0.10}$	$1.06_{-0.29}^{+0.29}$	$0.34_{-0.12}^{+0.13}$	$0.26_{-0.14}^{+0.49}$	$0.67_{-0.13}^{+1.33}$
	$10.0_{-5.26}^{+19.1}$	$22.4_{-4.13}^{+5.30}$	$49.5_{-8.40}^{+10.0}$	$1.21_{-0.34}^{+0.69}$	$0.75_{-0.49}^{+0.28}$	$0.15_{-0.08}^{+0.08}$	0.97
NGC 2110	$0.90_{-0.01}^{+0.01}$	$0.64_{-0.01}^{+0.01}$	$1.63_{-0.01}^{+0.01}$	$5.40_{-0.11}^{+0.10}$	$0.84_{-0.05}^{+0.05}$	$0.04_{-0.01}^{+0.01}$	$0.50_{-0.00}^{+0.26}$
	$0.18_{-0.01}^{+0.01}$	$63.8_{-12.9}^{+6.20}$	$31.7_{-11.7}^{+2.50}$	$0.36_{-0.03}^{+0.04}$	1.03
NGC 3227	$1.13_{-0.02}^{+0.02}$	$0.73_{-0.02}^{+0.02}$	$1.58_{-0.03}^{+0.03}$	$0.69_{-0.04}^{+0.03}$	$7.74_{-0.45}^{+0.46}$	$0.07_{-0.02}^{+0.01}$	$0.77_{-0.07}^{+0.87}$
	$0.56_{-0.12}^{+0.07}$	$51.6_{-8.00}^{+12.3}$	20.0 (fixed)	$0.66_{-0.06}^{+0.07}$	1.22
NGC 3281	$0.92_{-0.07}^{+0.07}$	$3.00_{-0.27}^{+0.28}$	$1.50_{-0.00}^{+0.05}$	$0.19_{-0.01}^{+0.04}$	$1.54_{-0.31}^{+0.31}$	$0.66_{-0.17}^{+0.38}$	$2.00_{-1.21}^{+0.00}$
	$9.79_{-2.56}^{+5.70}$	$38.0_{-6.50}^{+9.10}$	$20.1_{-0.10}^{+6.40}$	$2.63_{-0.51}^{+0.67}$	$0.37_{-0.14}^{+0.32}$	$0.34_{-0.18}^{+0.31}$	1.23
NGC 5506	$1.02_{-0.01}^{+0.01}$	$2.02_{-0.03}^{+0.04}$	$1.84_{-0.01}^{+0.02}$	$1.88_{-0.06}^{+0.06}$	$1.23_{-0.12}^{+0.12}$	$0.03_{-0.01}^{+0.01}$	$0.50_{-0.00}^{+1.50}$
	$12.5_{-3.75}^{+3.70}$	$24.6_{-2.58}^{+2.70}$	$33.4_{-10.6}^{+2.77}$	$1.78_{-0.36}^{+0.30}$	1.08
NGC 5643	$1.19_{-0.11}^{+0.12}$	$2.57_{-1.63}^{+2.50}$	$1.68_{-0.17}^{+0.18}$	$0.23_{-0.12}^{+0.53}$	$6.30_{-3.94}^{+5.48}$	$2.36_{-0.58}^{+2.24}$	$2.00_{-0.53}^{+0.00}$
	$1.50_{-0.36}^{+1.40}$	$34.8_{-18.5}^{+35.2}$	74.0 (fixed)	$2.70_{-0.51}^{+0.81}$	$0.25_{-0.06}^{+0.12}$	$1.17_{-0.59}^{+0.83}$	0.99
NGC 5728	$0.99_{-0.11}^{+0.12}$	$0.56_{-0.07}^{+0.08}$	$1.50_{-0.00}^{+0.05}$	$0.45_{-0.03}^{+0.13}$	$0.83_{-0.28}^{+0.14}$	$0.95_{-0.19}^{+0.28}$	$0.50_{-0.00}^{+0.20}$
	$2.00_{-0.40}^{+0.58}$	$60.0_{-13.5}^{+10.0}$	80.0 (fixed)	$1.20_{-0.32}^{+0.08}$	$0.56_{-0.27}^{+0.17}$	$0.31_{-0.10}^{+0.30}$	1.00
NGC 7172	$0.98_{-0.01}^{+0.01}$	$1.08_{-0.02}^{+0.02}$	$1.76_{-0.10}^{+0.02}$	$2.05_{-0.11}^{+0.11}$	$0.00_{-0.02}^{+0.08}$	$0.09_{-0.02}^{+0.18}$	$0.50_{-0.00}^{+1.50}$
	$5.26_{-1.40}^{+10.3}$	$12.6_{-2.60}^{+3.00}$	$66.9_{-6.44}^{+3.51}$	$1.13_{-0.16}^{+0.50}$	$0.59_{-0.27}^{+0.48}$	$0.10_{-0.04}^{+0.08}$	1.02
NGC 7582	$1.10_{-0.09}^{+0.09}$	$0.10_{-0.07}^{+0.01}$	$1.77_{-0.07}^{+0.08}$	$1.05_{-0.22}^{+0.32}$	$1.20_{-0.25}^{+0.27}$	$0.31_{-0.13}^{+0.16}$	$1.47_{-0.97}^{+0.53}$
	$7.29_{-3.00}^{+3.64}$	$25.8_{-3.60}^{+10.5}$	$41.4_{-5.80}^{+7.10}$	$0.64_{-0.13}^{+0.20}$	$0.76_{-0.11}^{+0.09}$	$0.47_{-0.12}^{+0.13}$	1.11
NGC 7674	$1.01_{-0.12}^{+0.13}$	$0.96_{-0.16}^{+0.20}$	$1.50_{-0.00}^{+0.07}$	$0.03_{-0.01}^{+0.01}$	$15.1_{-2.98}^{+3.02}$	$0.24_{-0.10}^{+0.22}$	$0.51_{-0.01}^{+1.49}$
	$10.0_{-4.10}^{+9.20}$	$39.9_{-8.80}^{+5.70}$	$20.0_{-0.00}^{+8.00}$	$2.76_{-0.98}^{+0.88}$	$0.71_{-0.12}^{+0.08}$	$0.34_{-0.07}^{+0.08}$	1.20

Note. Column (01): galaxy name. Column (02): relative normalization of Suzaku/BIXIS to Suzaku/FIXIS. Column (03): time variability constant. Column (04): photon index. Column (05): normalization of the direct component in units of 10^{-2} photons $\text{keV}^{-1} \text{cm}^{-2} \text{s}^{-1}$. Column (06): scattering fraction in percent. Column (07): hydrogen column density along the equatorial plane in units of 10^{24}cm^{-2} . Column (08): correction factor of the line-of-sight column density. Column (09): hydrogen column density along the line of sight in units of 10^{24}cm^{-2} . Column (10): torus angular width in units of degree. Column (11): inclination angle in units of degree. Column (12): relative normalization of the emission lines to the reflection component. Column (13): temperature of the apec model in units of keV. Column (14): normalization of the apec model in units of $10^{-18}/4\pi[D_{\Lambda}(1+z)]^2 \int n_e n_{\text{H}} dV$, where D_{Λ} is the angular diameter distance to the source in units of cm, and n_e and n_{H} are the electron and hydrogen densities in units of cm^{-3} . Column (15): reduced χ^2 .

Before that, we summarize the main driving spectral features that constrain these parameters in the analysis of the infrared and X-ray data. In the CLUMPY model (infrared), the depth of silicate absorption at $9.7 \mu\text{m}$ mainly determines the line-of-sight extinction (A_{V}). Ichikawa et al. (2015) considered the foreground extinction from the host galaxy for some objects (Ichikawa et al. 2015, Table 1). The spectral energy distribution (SED) slope from near- to mid-infrared wavelengths (the ratio of the mid- to near-infrared fluxes) constrains σ_{IR} ; a large σ_{IR} results in a steeper slope because emission from inner hot dust becomes more obscured (Nenkova et al. 2008b, Figure 8). Similarly, a larger inclination also makes the slope steeper, although the dependence is weak at $i_{\text{IR}} < 60^\circ$. Ichikawa et al. (2015) limited the range of i_{IR} when an independent constraint on the inclination is available (Ichikawa et al. 2015, Table 1).

High-quality broadband X-ray spectra enable us to separate the absorbed transmitted component and the reflection component from the torus. Unfortunately, the parameter dependencies of the reflection component in the XCLUMPY model are not simple (Tanimoto et al. 2019, Figure 2). Nevertheless, we roughly understand that (1) the flux ratio between the hard (>10 keV) and soft (<10 keV) bands mainly determines $N_{\text{H}}^{\text{Equ}}$ and (2) the spectral slope of the reflection component below 7.1 keV constrains σ . As described above, $N_{\text{H}}^{\text{LOS}}$ gives another constraint to the torus parameters through Equation (3). Note that we did not consider the foreground absorption adopted by

Ichikawa et al. (2015) in the X-ray spectral analysis. Assuming the $N_{\text{H}}/A_{\text{V}}$ ratio of the Galactic ISM, however, its estimated contribution is found to be negligible in $N_{\text{H}}^{\text{LOS}}$ or smaller than its uncertainty in all cases but NGC 5506.

To increase the sample, we include the Circinus galaxy (Tanimoto et al. 2019)¹⁴ and NGC 5135 (Yamada et al. 2020)¹⁵ fitted with the XCLUMPY model in the following discussions. Figure 2 plots the relations between (a) the torus angular width obtained from the X-ray spectrum (σ_{X}) and that from the infrared spectrum (σ_{IR}), and (b) the inclination angle obtained from the X-ray spectrum (i_{X}) and that from the infrared spectrum (i_{IR}), (c) the hydrogen column density along the line of sight obtained from the X-ray spectrum ($N_{\text{H}}^{\text{LOS}}$) and the V-band extinction along the line of sight from the infrared spectrum ($A_{\text{V}}^{\text{LOS}}$), and (d) the hydrogen column density along the equatorial plane obtained from the X-ray spectrum ($N_{\text{H}}^{\text{Equ}}$) and the V-band extinction along the equatorial plane obtained from the infrared spectrum ($A_{\text{V}}^{\text{Equ}}$). Note that we fix the inclination angles of three objects: NGC 3227, NGC 5643, and NGC 5728.

¹⁴ We have reanalyzed the same X-ray spectra of the Circinus galaxy as presented in Tanimoto et al. (2019) by introducing the α parameter, which was not considered in the original analysis. We have confirmed $\alpha = 0.95_{-0.05}^{+0.13}$.

¹⁵ Yamada et al. (2020) assume $\alpha = 1$ because it cannot be determined well due to the limited photon statistics of the spectra.

Table 4
Fluxes and Luminosities

Galaxy Name (1)	$\log F_{2-10}$ (2)	$\log L_{2-10}$ (3)	$\log M_{\text{BH}}/M_{\odot}$ (4)	$\log \lambda_{\text{Edd}}$ (5)	M_{BH} Reference (6)
IC 5063	-11.1	43.0	8.45	-2.29	(1)
NGC 2110	-9.90	43.5	9.25	-2.53	(2)
NGC 3227	-10.7	42.0	7.18	-1.94	(2)
NGC 3281	-11.4	42.4	8.00	-2.38	(3)
NGC 5506	-10.0	42.7	7.87	-1.96	(4)
NGC 5643	-11.9	41.4	7.05	-2.41	(1)
NGC 5728	-11.8	42.7	8.07	-2.18	(2)
NGC 7172	-10.4	43.1	8.45	-2.15	(2)
NGC 7582	-11.6	42.3	7.74	-2.19	(2)
NGC 7674	-12.1	42.4	8.50	-2.87	(5)

Note. Column (1): galaxy name. Column (2): logarithmic observed flux in 2–10 keV (Suzaku/FIXIS). Column (3): logarithmic intrinsic luminosity in 2–10 keV. Column (4): logarithmic black hole mass. Column (5): logarithmic Eddington ratio ($\lambda_{\text{Edd}} = L_{\text{bol}}/L_{\text{Edd}}$). Here we obtained the bolometric luminosity as $L_{\text{bol}} = 20L_{2-10}$ and defined the Eddington luminosity as $L_{\text{Edd}} = 1.25 \times 10^{38} M_{\text{BH}}/M_{\odot}$. Column (6): reference of the black hole mass.

References. (1) van den Bosch (2016). (2) Koss et al. (2017). (3) Panessa et al. (2015). (4) Izumi et al. (2016). (5) Haan et al. (2011).

Figure 2(a) indicates that σ_{IR} is systematically larger than σ_{X} . Here we recall that the X-ray spectra trace all material including gas and dust in a rather unbiased manner, while the infrared data trace only dust in a temperature-dependent way. This means that the apparent dust distribution as seen in the infrared band is effectively more extended in the vertical direction to the equatorial plane than the gas distribution. We infer that this can be explained by the contribution by the dusty polar outflows to the observed infrared flux, which are commonly observed in nearby AGNs by infrared interferometric observations (e.g., Tristram et al. 2014; Lyu & Rieke 2018). Because the CLUMPY model does not include such a polar dust component, this may lead to an overestimate of the actual angular width of the torus. The mean temperature of polar dust is lower than that of hot dust in the innermost torus region, because of its larger distance from the SMBH. Hence, it works to make the mid- to near-infrared flux ratio larger, leading to a large σ_{IR} value (see above). This effect becomes more significant when the infrared flux from the torus is reduced due to extinction by dust in outer cooler regions (such as circumnuclear disks) compared with the prediction by CLUMPY. Such flux reduction is predicted by radiative hydrodynamical simulations, which show a “shadow” region around the equatorial plane in the mid-infrared image (Wada et al. 2016).

By contrast, the X-ray results are less affected by the polar outflows. This is because the mass carried by the polar outflows is much smaller than that contained in the torus itself (Wada et al. 2016) and because hard X-rays emitted at the central engine can penetrate through the torus. Liu et al. (2019) examined the X-ray signatures of the polar outflows with ray-tracing simulations and found that it only contributed to the X-ray spectrum below 2 keV, such as Si K α emission lines, and not to Fe K α emission lines and hard X-ray continuum above 10 keV. Hence, we expect that X-ray results mainly trace the equatorial dusty torus distribution. We recall that a reflection component with an Fe K α line from an extended region of $\gg 1$ pc scale may be contained in our X-ray spectra, the contribution of which differs object to object, for instance, a few percent and $\approx 30\%$ of the Fe K α line fluxes in Circinus (Kawamuro et al. 2019) and NGC 1068 (Bauer et al. 2015), respectively. This would lead to an overestimate of σ_{X} if the

column density of the extended Fe K α region is comparable to that in the torus, whereas the effect is less significant for σ_{IR} because the infrared data are better localized ($< 1''$) than the X-ray data ($> 10''$). Hence, the differences between σ_{X} and σ_{IR} would be even enhanced after correcting them for this possible effect.

Figure 3(b) shows that the correlation between i_{X} and i_{IR} is not good after excluding the objects for which we have assumed $i_{\text{X}} = i_{\text{IR}}$ in the X-ray spectral analysis. We infer that this is because it is difficult to constrain i_{IR} from the infrared data because of its small dependence on the SED at low inclinations (see above). Although the X-ray results are inevitably subject to coupling with the α parameter (see Equation (3)), we have taken it into account in estimating the uncertainties. In the following discussion, we refer to i_{X} as an estimate of the inclination.

Because the line-of-sight extinction is more directly determined from the X-ray and infrared data through photoelectric absorption and silicate absorption, respectively, we mainly focus on the correlation between $N_{\text{H}}^{\text{LOS}}$ and $A_{\text{V}}^{\text{LOS}}$ (Figure 2(c)). The mean value of $N_{\text{H}}^{\text{LOS}}/A_{\text{V}}^{\text{LOS}}$ is close to that of the Galactic ISM: $N_{\text{H}}/A_{\text{V}} = 1.87 \times 10^{21} \text{ cm}^{-2} \text{ mag}^{-1}$ (Draine 2003). This is consistent with the results of Burtscher et al. (2016), who investigated $N_{\text{H}}^{\text{LOS}}/A_{\text{V}}^{\text{LOS}}$ utilizing colors of dust. This result would be little affected even if we overestimated $N_{\text{H}}^{\text{LOS}}$ of NGC 5506 due to the possible foreground absorption (see above). We note that Figures 2(c) and (d) indicate scatter (≈ 1 dex) in the ratio between the hydrogen column density and the V-band extinction, both along the line of sight and along the equatorial plane.

With the presence of dusty polar outflows, the value of A_{V} obtained should be a flux-weighted average from two different regions, the polar outflows and the torus. Because the polar outflows are located above the torus, their extinction is smaller than that for the torus itself. As discussed in Section 5.2, the relative contribution from dusty polar outflows to the total infrared flux increases with the inclination. Hence, the A_{V} value may be largely underestimated compared to that toward the torus at high-inclination systems, leading to large $N_{\text{H}}^{\text{LOS}}/A_{\text{V}}^{\text{LOS}}$ values, even without invoking a significant amount of dust-free gas inside the dust sublimation radius (e.g., Davies et al. 2015; Ichikawa et al. 2019; Kawakatu et al. 2020).

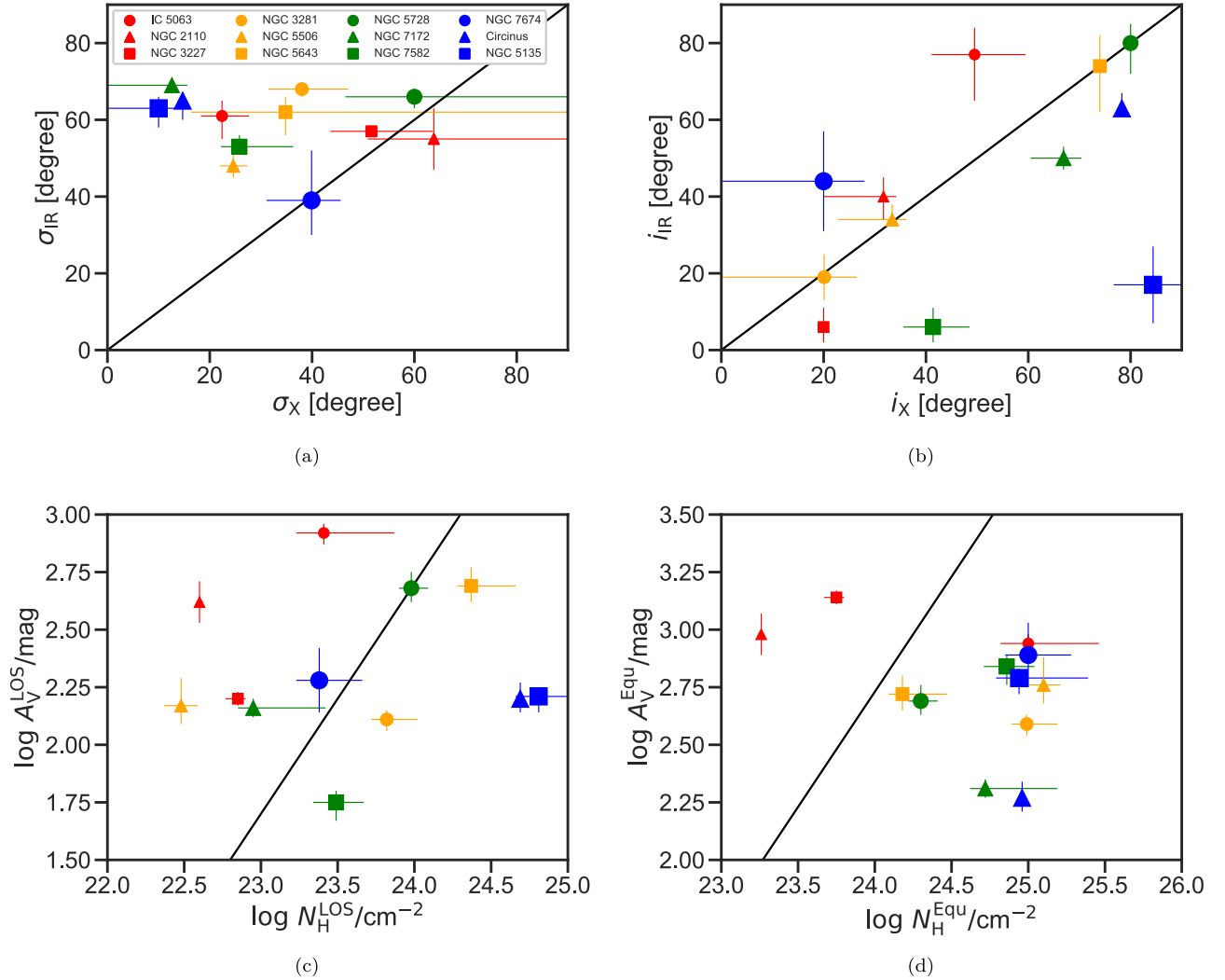


Figure 2. (a) Correlation between the torus angular width obtained from the X-ray spectrum (σ_{X}) and that from the infrared spectrum (σ_{IR}). The black line shows $\sigma_{\text{X}} = \sigma_{\text{IR}}$. (b) Correlation between the inclination angle obtained from the X-ray spectrum (i_{X}) and that from the infrared spectrum (i_{IR}). The black line shows $i_{\text{X}} = i_{\text{IR}}$. (c) Correlation between the hydrogen column density along the line of sight obtained from the X-ray spectrum ($N_{\text{H}}^{\text{LOS}}$) and the V-band extinction along the line of sight from the infrared spectrum ($A_{\text{V}}^{\text{LOS}}$). (d) Correlation between the hydrogen column density along the equatorial plane obtained from the X-ray spectrum ($N_{\text{H}}^{\text{Equ}}$) and the V-band extinction along the equatorial plane from the infrared spectrum ($A_{\text{V}}^{\text{Equ}}$). The black line corresponds to the Galactic value $N_{\text{H}}/A_{\text{V}} = 1.87 \times 10^{21} \text{ cm}^{-2} \text{ mag}^{-1}$ (Draine 2003). Note that we fix i_{X} to i_{IR} for NGC 3227, NGC 5643, and NGC 5728. For NGC 3227, we fix i_{X} at 20° , the lower boundary value in the XCLUMPY model, whereas $i_{\text{IR}} = 6^\circ$.

If we exclude the two highest-inclination ($i \geq 70^\circ$) objects (Circinus galaxy and NGC 5135) as exceptions, more than half of our sample seems to have a “dust-rich” circumnuclear environment compared with the Galactic ISM; this conclusion is even strengthened if we correct for the contribution from the polar outflows. Ogawa et al. (2019) found such dust-rich AGNs by applying XCLUMPY to the broadband X-ray spectra of two Seyfert 1 galaxies. This trend is opposite to that reported for some AGNs that show cold absorption in X-rays and optical broad emission lines (e.g., Maiolino et al. 2001a, 2001b).

5.3. Origin of the Torus Parameter Differences between the X-Ray and Infrared

To reinforce our interpretation of the torus parameter differences between the X-ray and infrared, Figure 3 plots $\sigma_{\text{IR}} - \sigma_{\text{X}}$ and $N_{\text{H}}^{\text{LOS}}/A_{\text{V}}^{\text{LOS}}$ as a function of inclination (i_{X}). Here we exclude the three objects whose i_{X} cannot be well

determined from the X-ray spectra (NGC 3227, NGC 5643, and NGC 5728).

Figure 3(a) indicates that $\sigma_{\text{IR}} - \sigma_{\text{X}}$ correlates with i_{X} . We find that the X-ray spectral fit shows a positive degeneracy between σ_{X} and i_{X} , which even strengthens the presence of this correlation. The tendency still exists even if we exclude NGC 3281 and NGC 7674, which have $i_{\text{X}} \sim 20^\circ$ degree with a reduced χ^2 of ≈ 1.2 . The result is expected from radiative hydrodynamics simulations, which showed that the relative contribution from the dusty polar outflow to the total observed mid-infrared flux increases with inclination (Wada et al. 2016, Figure 5b).¹⁶ This supports the fact σ_{IR} is largely overestimated at high-inclination systems.

¹⁶ Although the matter distribution assumed in the X/CLUMPY models is too simple compared with that in the Wada et al. (2016) model, it would give a good first-order approximation for the broad column-density peak around the equatorial plane (Wada et al. 2016, Figure 4).

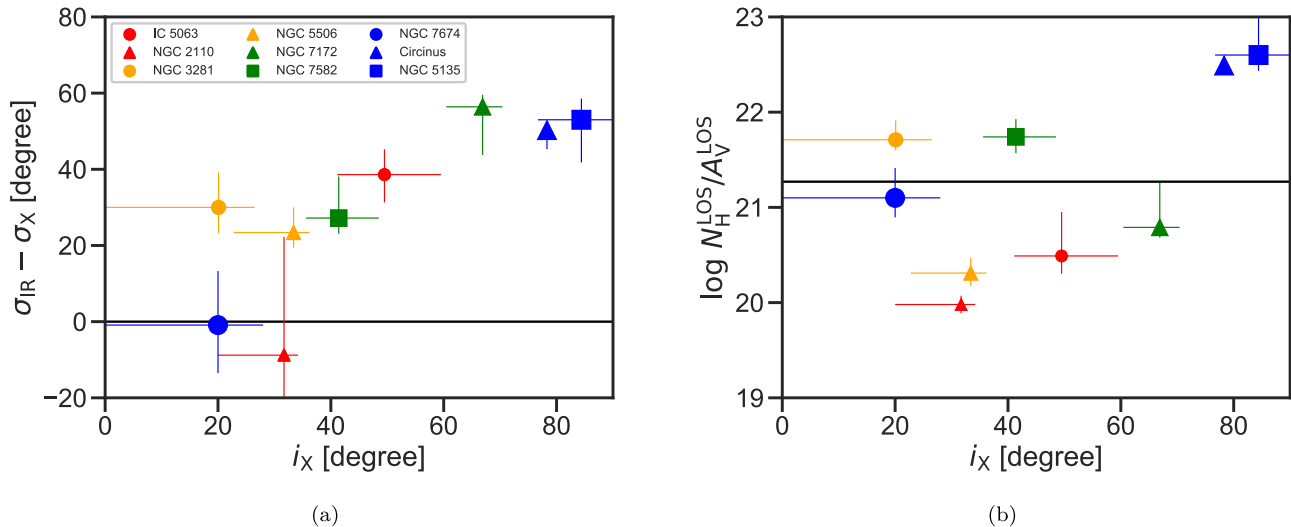


Figure 3. (a) $\sigma_{\text{IR}} - \sigma_{\text{X}}$ vs. i_{X} . The black line shows $\sigma_{\text{X}} = \sigma_{\text{IR}}$. (b) $\log N_{\text{H}}^{\text{LOS}} / A_{\text{V}}^{\text{LOS}}$ vs. the inclination angle obtained from the X-ray spectrum (i_{X}). The black line corresponds to the Galactic value: $N_{\text{H}} / A_{\text{V}} = 1.87 \times 10^{21} \text{ cm}^{-2} \text{ mag}^{-1}$ (Draine 2003).

Figure 3(b) shows that the two highest-inclination objects (Circinus Galaxy and NGC 5135) have especially large $N_{\text{H}}^{\text{LOS}} / A_{\text{V}}^{\text{LOS}}$ values. As mentioned above, this is because A_{V} in the torus is likely underestimated by the contribution of the dusty polar outflows that are subject to smaller extinction. At lower inclinations, this effect becomes less important, and the observed ratio of $N_{\text{H}}^{\text{LOS}} / A_{\text{V}}^{\text{LOS}}$ would correctly represent the gas-to-dust ratio of matter in the line of sight if the travel paths of X-ray and infrared radiation are the same. Our results imply a large object-to-object variation (~ 1 dex) in the gas-to-dust ratio of an AGN torus with a mean close to the Galactic value.

6. Conclusion

1. We apply our X-ray spectral model from a clumpy torus (XCLUMPY; Tanimoto et al. 2019) to the X-ray spectra of 10 obscured AGNs observed with both Suzaku and NuSTAR.
2. The torus angular widths obtained from the infrared spectra (σ_{IR}) are systematically larger than those from the X-ray spectra (σ_{X}). Their difference is larger in higher-inclination objects. These results can be explained by the significant contribution of the dusty polar outflows to the infrared flux, as observed in infrared interferometric observations and predicted by theoretical simulations.
3. The ratios between the line-of-sight hydrogen column density and V-band extinction ($N_{\text{H}}^{\text{LOS}} / A_{\text{V}}^{\text{LOS}}$) show a large scatter ($\simeq 1$ dex) around the Galactic ISM value, suggesting that a large fraction of AGNs have dust-rich circumnuclear environments.

This work was financially supported by the Grant-in-Aid for JSPS fellows for young researchers 17J06407 (A.T.) and Scientific Research 17K05384 and 20H01946 (Y.U.) and 18H05861 (H.O.). This research has made use of data and/or software provided by the High Energy Astrophysics Science Archive Research Center (HEASARC), which is a service of the Astrophysics Science Division at NASA/GSFC and the High Energy Astrophysics Division of the Smithsonian Astrophysical Observatory. This research has also made use of the NASA/IPAC Extragalactic Database (NED), which is operated by the Jet Propulsion Laboratory, California Institute

of Technology, under contract with the National Aeronautics and Space Administration.

Facilities: Suzaku (701030030, 701079010, 702010010, 702052040, 703022050, 703030010, 703033010, 704010010, 707034010, 708023010); NuSTAR (60001151002, 60061061002, 60061201002, 60061256002, 60061302002, 60061308002, 60061323002, 60061362002, 60201003002, 60202002002).

Software: HEASoft 6.26 (HEASARC 2018), XSPEC (Arnaud 1996).

ORCID iDs

Atsushi Tanimoto <https://orcid.org/0000-0002-0114-5581>
 Yoshihiro Ueda <https://orcid.org/0000-0001-7821-6715>
 Shoji Ogawa <https://orcid.org/0000-0002-5701-0811>
 Satoshi Yamada <https://orcid.org/0000-0002-9754-3081>
 Kohei Ichikawa <https://orcid.org/0000-0002-4377-903X>

References

- Alonso-Herrero, A., Pereira-Santaella, M., Rieke, G. H., & Rigopoulou, D. 2012a, *ApJ*, 744, 2
- Alonso-Herrero, A., Ramos Almeida, C., Mason, R., et al. 2011, *ApJ*, 736, 82
- Alonso-Herrero, A., Roche, P. F., Esquej, P., et al. 2013, *ApJL*, 779, L14
- Alonso-Herrero, A., Sánchez-Portal, M., Ramos Almeida, C., et al. 2012b, *MNRAS*, 425, 311
- Anders, E., & Grevesse, N. 1989, *GeCoA*, 53, 197
- Antonucci, R. 1993, *ARA&A*, 31, 473
- Arévalo, P., Bauer, F. E., Puccetti, S., et al. 2014, *ApJ*, 791, 81
- Arnaud, K. A. 1996, *adass V*, 101, 17
- Audibert, A., Riffel, R., Sales, D. A., Pastoriza, M. G., & Ruschel-Dutra, D. 2017, *MNRAS*, 464, 2139
- Baloković, M., Brightman, M., Harrison, F. A., et al. 2018, *ApJ*, 854, 42
- Bauer, F. E., Arévalo, P., Walton, D. J., et al. 2015, *ApJ*, 812, 116
- Bianchi, S., Piconcelli, E., Chiaberge, M., et al. 2009, *ApJ*, 695, 781
- Buchner, J., Brightman, M., Nandra, K., Nikutta, R., & Bauer, F. E. 2019, *A&A*, 629, A16
- Burtscher, L., Davies, R. I., Graciá-Carpio, J., et al. 2016, *A&A*, 586, A28
- Davies, R. I., Burtscher, L., Rosario, D., et al. 2015, *ApJ*, 806, 127
- Draine, B. T. 2003, *ARA&A*, 41, 241
- Fabbiano, G., Elvis, M., Paggi, A., et al. 2017, *ApJL*, 842, L4
- Fukazawa, Y., Hiragi, K., Yamazaki, S., et al. 2011, *ApJ*, 743, 124
- Fukazawa, Y., Mizuno, T., Watanabe, S., et al. 2009, *PASJ*, 61, S17
- Fuller, L., Lopez-Rodriguez, E., Packham, C., et al. 2016, *MNRAS*, 462, 2618
- Fuller, L., Lopez-Rodriguez, E., Packham, C., et al. 2019, *MNRAS*, 483, 3404
- Furui, S., Fukazawa, Y., Odaka, H., et al. 2016, *ApJ*, 818, 164

- Gandhi, P., Annuar, A., Lansbury, G. B., et al. 2017, *MNRAS*, **467**, 4606
- García, J., Dauser, T., Reynolds, C. S., et al. 2013, *ApJ*, **768**, 146
- García-Berete, I., Ramos Almeida, C., Acosta-Pulido, J. A., et al. 2015, *MNRAS*, **449**, 1309
- García-Berete, I., Ramos Almeida, C., Alonso-Herrero, A., et al. 2019, *MNRAS*, **486**, 4917
- González-Martín, O., Rodríguez-Espinosa, J. M., Díaz-Santos, T., et al. 2013, *A&A*, **553**, A35
- Haan, S., Surace, J. A., Armus, L., et al. 2011, *AJ*, **141**, 100
- Harrison, F. A., Craig, W. W., Christensen, F. E., et al. 2013, *ApJ*, **770**, 103
- Heckman, T. M., & Best, P. N. 2014, *ARA&A*, **52**, 589
- Hönig, S. F., & Beckert, T. 2007, *MNRAS*, **380**, 1172
- Hönig, S. F., Beckert, T., Ohnaka, K., & Weigelt, G. 2006, *A&A*, **452**, 459
- Hönig, S. F., Kishimoto, M., Antonucci, R., et al. 2012, *ApJ*, **755**, 149
- Ichikawa, K., Packham, C., Ramos Almeida, C., et al. 2015, *ApJ*, **803**, 57
- Ichikawa, K., Ricci, C., Ueda, Y., et al. 2019, *ApJ*, **870**, 31
- Ikeda, S., Awaki, H., & Terashima, Y. 2009, *ApJ*, **692**, 608
- Ishisaki, Y., Maeda, Y., Fujimoto, R., et al. 2007, *PASJ*, **59**, 113
- Izumi, T., Kawakatu, N., & Kohno, K. 2016, *ApJ*, **827**, 81
- Kallman, T., Evans, D. A., Marshall, H., et al. 2014, *ApJ*, **780**, 121
- Kawakatu, N., Wada, K., & Ichikawa, K. 2020, *ApJ*, **889**, 84
- Kawamuro, T., Izumi, T., & Imanishi, M. 2019, *PASJ*, **71**, 68
- Kawamuro, T., Ueda, Y., Tazaki, F., Ricci, C., & Terashima, Y. 2016a, *ApJS*, **225**, 14
- Kawamuro, T., Ueda, Y., Tazaki, F., Terashima, Y., & Mushotzky, R. 2016b, *ApJ*, **831**, 37
- Kokubun, M., Makishima, K., Takahashi, T., et al. 2007, *PASJ*, **59**, 53
- Kormendy, J., & Ho, L. C. 2013, *ARA&A*, **51**, 511
- Koss, M., Trakhtenbrot, B., Ricci, C., et al. 2017, *ApJ*, **850**, 74
- Koyama, K., Tsunemi, H., Dotani, T., et al. 2007, *PASJ*, **59**, 23
- Krolik, J. H., & Begelman, M. C. 1988, *ApJ*, **329**, 702
- Laor, A., & Draine, B. T. 1993, *ApJ*, **402**, 441
- Liu, J., Hönig, S. F., Ricci, C., & Paltani, S. 2019, *MNRAS*, **490**, 4344
- Liu, Y., & Li, X. 2014, *ApJ*, **787**, 52
- Lopez-Rodriguez, E., Fuller, L., Alonso-Herrero, A., et al. 2018, *ApJ*, **859**, 99
- Lyu, J., & Rieke, G. H. 2018, *ApJ*, **866**, 92
- Magdziarz, P., & Zdziarski, A. A. 1995, *MNRAS*, **273**, 837
- Maiolino, R., Marconi, A., & Oliva, E. 2001a, *A&A*, **365**, 37
- Maiolino, R., Marconi, A., Salvati, M., et al. 2001b, *A&A*, **365**, 28
- Marchesi, S., Ajello, M., Zhao, X., et al. 2019, *ApJ*, **872**, 8
- Marinucci, A., Matt, G., Bianchi, S., et al. 2015, *MNRAS*, **447**, 160
- Mateos, S., Carrera, F. J., Barcons, X., et al. 2017, *ApJL*, **841**, L18
- Matt, G., Baloković, M., Marinucci, A., et al. 2015, *MNRAS*, **447**, 3029
- Mitsuda, K., Bautz, M., Inoue, H., et al. 2007, *PASJ*, **59**, S1
- Murphy, K. D., & Yaqoob, T. 2009, *MNRAS*, **397**, 1549
- Nenkova, M., Sirocky, M. M., Ivezić, Ž., & Elitzur, M. 2008a, *ApJ*, **685**, 147
- Nenkova, M., Sirocky, M. M., Nikutta, R., Ivezić, Ž., & Elitzur, M. 2008b, *ApJ*, **685**, 160
- Netzer, H. 2015, *ARA&A*, **53**, 365
- Noda, H., Makishima, K., Yamada, S., et al. 2014, *ApJ*, **794**, 2
- Odaka, H., Aharonian, F., Watanabe, S., et al. 2011, *ApJ*, **740**, 103
- Odaka, H., Yoneda, H., Takahashi, T., & Fabian, A. 2016, *MNRAS*, **462**, 2366
- Ogawa, S., Ueda, Y., Yamada, S., Tanimoto, A., & Kawaguchi, T. 2019, *ApJ*, **875**, 115
- Panessa, F., Tarchi, A., Castangia, P., et al. 2015, *MNRAS*, **447**, 1289
- Protassov, R., van Dyk, D. A., Connors, A., Kashyap, V. L., & Siemiginowska, A. 2002, *ApJ*, **571**, 545
- Ramos Almeida, C., Alonso-Herrero, A., Esquej, P., et al. 2014a, *MNRAS*, **445**, 1130
- Ramos Almeida, C., Alonso-Herrero, A., Levenson, N. A., et al. 2014b, *MNRAS*, **439**, 3847
- Ramos Almeida, C., Dicken, D., Tadhunter, C., et al. 2011a, *MNRAS*, **413**, 2358
- Ramos Almeida, C., Levenson, N. A., Alonso-Herrero, A., et al. 2011b, *ApJ*, **731**, 92
- Ramos Almeida, C., Levenson, N. A., Rodríguez Espinosa, J. M., et al. 2009, *ApJ*, **702**, 1127
- Ramos Almeida, C., & Ricci, C. 2017, *NatAs*, **1**, 679
- Ramos Almeida, C., Sánchez-Portal, M., Pérez García, A. M., et al. 2011c, *MNRAS*, **417**, L46
- Ricci, C., Ho, L. C., Fabian, A. C., et al. 2018, *MNRAS*, **480**, 1819
- Rivers, E., Markowitz, A., Rothschild, R., et al. 2014, *ApJ*, **786**, 126
- Schoonjans, T., Brunetti, A., Golosio, B., et al. 2011, *AcSpe*, **66**, 776
- Takahashi, T., Abe, K., Endo, M., et al. 2007, *PASJ*, **59**, 35
- Tanimoto, A., Ueda, Y., Kawamuro, T., et al. 2018, *ApJ*, **853**, 146
- Tanimoto, A., Ueda, Y., Odaka, H., et al. 2019, *ApJ*, **877**, 95
- Tazaki, F., Ueda, Y., Terashima, Y., & Mushotzky, R. F. 2011, *ApJ*, **738**, 70
- Tristram, K. R. W., Burtscher, L., Jaffe, W., et al. 2014, *A&A*, **563**, A82
- Urry, C. M., & Padovani, P. 1995, *PASP*, **107**, 803
- van den Bosch, R. C. E. 2016, *ApJ*, **831**, 134
- Wada, K., Schartmann, M., & Meijerink, R. 2016, *ApJL*, **828**, L19
- Willingale, R., Starling, R. L. C., Beardmore, A. P., Tanvir, N. R., & O'Brien, P. T. 2013, *MNRAS*, **431**, 394
- Yamada, S., Ueda, Y., Tanimoto, A., et al. 2020, arXiv:2005.08718